

1 **Two years of satellite-based carbon dioxide emission quantification at the world's** 2 **largest coal-fired power plants**

3 Daniel H. Cusworth^{1,2}, Andrew K. Thorpe³, Charles E. Miller³, Alana K. Ayasse¹, Ralph Jiorle¹,
4 Riley M. Duren^{1,2,3}, Ray Nassar⁴, Jon-Paul Mastrogiamomo⁵, and Robert R. Nelson³

5 ¹Carbon Mapper, Pasadena, CA, USA

6 ²Arizona Institutes for Resilience, University of Arizona, Tucson, AZ, USA

7 ³Jet Propulsion Laboratory, California Institute of Technology, Pasadena, CA, USA

8 ⁴Environment & Climate Change Canada, [Toronto, ON, Canada](#)

9 ⁵University of Toronto, [Toronto, ON, Canada](#)

10

11 Corresponding Author: Daniel H. Cusworth (dan@carbonmapper.org)

12

13 **Abstract**

14 Carbon dioxide (CO₂) emissions from combustion sources are uncertain in many places
15 across the globe. Satellites have the ability to detect and quantify emissions from large CO₂ point
16 sources, including coal-fired power plants. In this study, we ~~tasked them~~ made observations with the
17 PRecursores IperSpettrale della Missione Applicativa (PRISMA) satellite imaging spectrometer and
18 the Orbiting Carbon Observatory-3 (OCO-3) instrument onboard the International Space Station at
19 over 30 coal-fired power plants routinely between 2021-2022. CO₂ plumes were detected in 50% of
20 acquired PRISMA scenes, which is consistent with the combined influence of viewing parameters
21 on detection (solar illumination, surface reflectance) and unknown factors (like daily operational
22 status). We compare satellite-derived emission rates to *in situ* stack emission observations and find
23 average agreement to within 27% for PRISMA and 30% for OCO-3, though more observations are
24 needed to robustly characterize the error. We highlight two examples of fusing PRISMA with OCO-
25 2 and OCO-3 observations in South Africa and India. For India, we acquired PRISMA and OCO-3

26 observations on the same day and use the high spatial resolution capability of PRISMA (30 m
27 spatial/pixel resolution) to partition relative contributions of two distinct emitting power plants to the
28 net emission. Though an encouraging start, two years of ~~tasking these observations from these~~
29 satellites did not produce sufficient observations to estimate annual average emission rates within
30 low (<15%) uncertainties. However, as the constellation of CO₂-observing satellites is poised to
31 significantly improve in the coming decade, this study offers an approach to leverage multiple
32 observation platforms to better ~~understand—quantify and characterize uncertainty for~~ large
33 anthropogenic emission sources.

34

35 **1 Introduction**

36 Anthropogenic carbon dioxide (CO₂) emissions are dominated by strong discrete point
37 sources: ~~power and other industrial combustion are estimated to make up 59% of global~~
38 ~~anthropogenic CO₂ emissions with transport, buildings, and other sources making up the remaining~~
39 ~~20%, 9%, and 12%, respectively that result from energy generation at energy supply facilities (e.g.,~~
40 ~~power plants) and industrial facilities~~ (Crippa et al., ~~2019~~2022). Fossil fuel combustion is the largest
41 contributor to warming trends globally since the pre-industrial era (IPCC, 2021). However, there
42 remains uncertainty in the total magnitude of emissions from these sectors as bottom-up emission
43 estimates rely on reported emission factors and activity data, which may vary in granularity and
44 quality across countries and provinces (Hong et al., 2017; Guan et al., 2017). Accurate CO₂ emission
45 quantification is important in light of the Paris Agreement, as participating countries must develop
46 plans and report progress to reduce their country's greenhouse gas (GHG) emissions (UN, 2015).
47 Leveraging atmospheric measurements, particularly satellite remote sensing, can help reduce
48 uncertainty in facility-level CO₂ emission estimates, provided that the observations are accurate and

49 sufficiently sample the facility in time (Hill and Nassar, 2019). Deployed systematically with robust
50 error characterization, this system could be an anchor towards assessing and verifying anticipated
51 CO₂ emission reductions as part of national and global GHG emission reduction plans and
52 agreements.

53 Several studies have shown that atmospheric sounding satellites can accurately quantify some
54 point source CO₂ emissions from large individual coal-fired power plants. First, the Orbiting Carbon
55 Observatory-2 (OCO-2; Crisp et al., 2017) is a space-based instrument that observes solar
56 backscattered near-infrared radiance in the oxygen *A* band (758-772 nm; 0.04 nm spectral resolution),
57 the weak CO₂ band (1594-1619 nm; 0.08 nm spectral resolution), and strong CO₂ band (2042-2082
58 nm; 0.10 nm spectral resolution). OCO-2 views in nadir mode over land, while sun glint mode
59 increases the signal over water giving measurements both land and water, and target mode to target
60 specific validation or calibration sites. With its 10-km wide swath, $\leq 1.3 \times 2.25$ km² pixel resolution,
61 and better than 1.0 ppm precision for retrievals of the column-mean dry-air mole fraction of CO₂
62 (XCO₂) (Taylor et al., 2023), OCO-2 is sensitive to single CO₂ point sources that emit sufficiently
63 close to an OCO-2 orbital track and are spatially isolated from other major CO₂ sources. Using
64 satellite observations from OCO-2, Nassar et al. (2017) detected strong CO₂ enhancements in the
65 near vicinity of seven large coal-fired power plants and employed a Gaussian plume model emission
66 quantification technique to estimate emission rates for these facilities. Further study expanded the set
67 of facilities that could be quantified by OCO-2 (Nassar et al., 2021). Other studies have leveraged
68 the nitrogen dioxide (NO₂) retrieval capability and wide swath of the TROPOspheric Monitoring
69 Instrument (TROPOMI; van Geffen et al., 2020) to attribute and corroborate strong CO₂ signals seen
70 in OCO-2 observations (Hakkarainen et al., 2021; Reuter et al., 2019). The Orbiting Carbon
71 Observatory-3 (OCO-3; Eldering et al., 2019), the flight spare of OCO-2, has been on board the

72 International Space Station (ISS) since May 2019. Like OCO-2, it has been shown capable of
73 quantifying CO₂ power plant emissions. Nassar et al. (2022) analyzed nine successful OCO-3
74 acquisitions of the Bełchatów Power Station and found the variability in satellite-based emission
75 estimates agreed well with the variability in independently reported hourly power generation. Guo et
76 al., (2023) estimated emissions at Chinese power plants using OCO-2/3 and found close agreement
77 with emission inventories. OCO-3 is different than OCO-2 in that it has a two-axis Pointing Mirror
78 Assembly (PMA) for more agile pointing, allowing it to rapidly point off-nadir and take Snapshot
79 Area Mapping (SAM) mode observations over the course of two minutes. These SAMs are
80 approximately 80×80 km² collections of measurements and are typically over sites of interest
81 including cities, power plants, volcanoes, and flux towers.

82 Another class of remote sensing imaging spectrometers – sometimes also referred to as
83 hyperspectral imagers – also have been shown capable of detecting and quantifying strong CO₂
84 signals from large point sources. Thorpe et al. (2017) flew the Next-Generation Airborne/Infrared
85 Imaging Spectrometer (AVIRIS-NG) over a coal-fired power plant in Four Corners, New Mexico,
86 and detected strong CO₂ plumes. AVIRIS-NG observes a large range of solar backscattered radiance
87 (380-2500 nm), but at much coarser spectral resolution (5 nm), and high spatial resolution (e.g., 3 m
88 when flown at 3 km altitude). The much finer spatial resolution of AVIRIS-NG allows for improved
89 visualization of the origin of a CO₂ plume, but at the expense of fine precision for a single observed
90 CO₂ column. Still, Cusworth et al. (2021) analyzed a combination of AVIRIS-NG and the identically
91 built Global Airborne Observatory (GAO) at over 20 power plants in the U.S., quantified emission
92 rates, and found close agreement with continuous emissions monitoring (CEMS) hourly emission
93 observations. [From space, the PRecursorre IperSpettrale della Missione Applicativa \(PRISMA\),
94 launched in 2019, like AVIRIS-NG and GAO is sensitive to a large range of solar backscattered](#)

95 radiance (400-2500 nm), albeit at coarser spectral and spatial resolution (10 nm spectral resolution;
96 30 m spatial resolution; Loizzo et al., 2018). PRISMA is a tasked satellite instrument potentially
97 capable of hundreds of 30 × 30 km² observations per day, with equatorial crossing time of 10:30am,
98 and target revisit of seven days, though true revisit depends on tasking priorities of the system.
99 Cusworth et al. (2021) showed ~~The study also showed~~ a few examples of CO₂ plumes detected and
100 quantified with ~~the satellite PRISMA imaging spectrometer~~ PRISMA, with quantified emissions
101 similar in magnitude to reported CEMS emissions. (400-2500 nm; 10 nm spectral resolution; 30 m
102 spatial resolution; Loizzo et al., 2018).

103 The capacity for satellites to be leveraged as useful tools for reducing uncertainty in the global
104 CO₂ anthropogenic emission sector requires synthesis and routine tasking observations (i.e., tasking)
105 of a critical number of facilities. Therefore, in this study, we ~~tasked~~ made observations at a subset
106 of global coal-fired power plants routinely over the course of two years to probe detection limits,
107 emission quantification uncertainty, and data yields. We ~~tasked~~ observed these facilities with both
108 OCO-3 and PRISMA. To our knowledge, to date, this study represents the largest and longest-largest
109 satellite-based facility scale investigation of direct CO₂ emission quantification across a diverse set
110 of global power plants, and the first investigation to assess the capability of PRISMA to reliably
111 detect and quantify CO₂ point sources. The results, though not sufficient by themselves to reduce
112 uncertainty relative to bottom-up inventories significantly on an annual basis, show a path forward
113 for data fusion and synthesis of observations from the growing constellation of planned CO₂ sensing
114 satellites.

116 **2 Methods**

117 Table 1 lists the locations of all power plants we targeted during this study between 2021-
 118 2022 with PRISMA. OCO-3 includes a subset of these sites as well as other fossil fuel combustion
 119 sites as part of its list of possible targets. We identified coal-fired power plants to routinely target
 120 using a combination of bottom-up and top-down information. Bottom-up coal-fired power plant CO₂
 121 emission estimates rely on activity data, that usually includes permitted capacity of a power plant
 122 and its operational state; and emission factors, usually estimated from the composition of the coal
 123 that is combusted. Inventories, like the Global Energy Monitor (GEM), include this data for a large
 124 set of coal-fired power plants across the globe (GEM, 2023). From the GEM database, we gathered
 125 the top 10 largest bottom-up coal-fired power plants globally. We then gathered a list of top-down
 126 TROPOMI NO₂ combustion hotspots, as inferred by Beirle et al. (2021). We included an additional
 127 ~~non-overlapping~~ seven unique power plants using this dataset. Because the imaging scene size of
 128 PRISMA is 30 × 30 km², some adjacent smaller power plants were imaged simultaneously along
 129 with these larger power plants. In total, outside of the U.S., we made PRISMA observations at 27
 130 power plants. In the U.S., we chose 10 power plants to routinely target using reported EPA CEMS
 131 information (campd.epa.gov): five of the top 30 emitting power plants, and five progressively lower
 132 emitters, chosen so that we could assess satellite detection capabilities.

133

134 Table 1. Power plants that were targeted specifically by PRISMA in this study.

Power Plant Name	Country	Latitude	Longitude	Number clear-sky observations	Number plume detections	Minimum quantified CO ₂ emission (kt CO ₂ h ⁻¹)	Mean quantified CO ₂ emission (kt CO ₂ h ⁻¹)	Maximum quantified CO ₂ emission (kt CO ₂ h ⁻¹)
Mundra-Adani	India	22.82	69.55	12	7	0.49±0.07	1.09±0.19	1.76±0.32
Korba-Balco	India	22.40	82.74	5	1	NA*	NA	NA
PLN Paiton Baru	Indonesia	-7.71	113.57	4	2	NA	NA	NA
Craig	USA	40.46	-107.59	5	5	0.56±0.11	0.69±0.16	0.8±0.22

Cumberland	USA	36.39	-87.65	1	0	NA	NA	NA
Dry Fork	USA	44.39	-105.46	6	3	0.61±0.09	0.65±0.13	0.69±0.16
H L Spurlock	USA	38.70	-83.82	5	3	1.15±0.32	1.26±0.39	1.37±0.45
Ulsan Hanju (1)	South Korea	35.49	129.33	1	0	NA	NA	NA
Hasdeo	India	22.41	82.69	5	0	NA	NA	NA
Hekinan	Japan	34.83	136.96	6	4	0.72±0.47	3.88±1.09	8.35±2.14
Baotou-1	China	40.66	109.66	5	2	0.19±0.07	0.27±0.07	0.35±0.07
Kendal	South Africa	-26.09	28.97	7	2	0.85±0.13	0.85±0.13	0.85±0.13
NTPC Korba	India	22.39	82.68	6	1	1.28±0.27	1.28±0.27	1.28±0.27
Kriel	South Africa	-26.25	29.18	8	3	0.74±0.15	0.82±0.15	0.95±0.16
Labadie	USA	38.56	-90.84	4	4	0.73±0.18	0.73±0.18	0.73±0.18
Martin Lake	USA	32.26	-94.57	8	8	1.45±0.31	2±0.59	2.6±0.98
Matimba	South Africa	-23.67	27.61	11	8	0.33±0.05	0.72±0.16	1.14±0.32
Matla	South Africa	-26.28	29.14	8	3	0.33±0.05	0.77±0.15	1.37±0.27
Medupi	South Africa	-23.71	27.56	15	12	0.33±0.06	0.83±0.19	1.47±0.34
Mundra-Tata	India	22.82	69.53	12	5	0.38±0.09	0.74±0.13	1.32±0.21
Niederausem	Germany	51.00	6.67	1	0	NA	NA	NA
Oregon	USA	41.67	-83.44	5	1	NA	NA	NA
Paiton-3	Indonesia	-7.71	113.58	4	4	1.54±0.37	3.16±0.69	4.78±1.02
Rihand	India	24.03	82.79	8	5	0.83±0.17	0.99±0.26	1.36±0.38
Sanfeng	China	40.66	109.76	6	0	NA	NA	NA
Sasan	India	23.98	82.63	9	7	0.65±0.15	1.01±0.24	1.51±0.31
Sooner	USA	36.45	-97.05	6	3	1.05±0.22	1.05±0.22	1.05±0.22
Togtoh	China	40.20	111.36	2	2	0.25±0.06	0.91±0.17	1.58±0.27
Ulsan Hanju (2)	South Korea	35.47	129.38	1	0	NA	NA	NA
Vindhyachal	India	24.10	82.68	9	7	0.33±0.1	0.72±0.15	1.24±0.23
Waigaoqiao	China	31.36	121.60	6	1	NA	NA	NA
Yeosu Hanwha	South Korea	34.84	127.69	2	0	NA	NA	NA
Yosu	South Korea	34.83	127.67	2	0	NA	NA	NA
Al Zour	Kuwait	28.71	48.37	12	0	NA	NA	NA

135 *A value of “NA” indicates that no plumes were detected at this power plant or that the emission quantification
136 algorithm (described in Methods) failed to quantify an emission rate.
137

138 *2.2-1 PRISMA ~~tasking~~ observations and quantification*

139 PRISMA is a tasked satellite instrument, capable of collecting around 200 $30 \times 30 \text{ km}^2$ targets
 140 per day and has 20° pointing capability off nadir. Authenticated users can program single **task**
 141 **observation** requests through PRISMA’s web portal (prisma.asi.it), which currently allows for 13
 142 concurrent requests at a time per user. We specified two-week observing windows for each **task**
 143 request, and configured **tasks-requests** to collect if the scene-averaged solar zenith angle (SZA) was
 144 less than 70° and forecast meteorology anticipated less than 20% cloud cover. If the orbital
 145 configuration, weather, SZA align and there are no other conflicting or higher priority **task**-requests,
 146 PRISMA images a target.

147 For each acquired PRISMA image, we performed XCO₂ retrievals on all pixels within a 2.5
 148 km radius around the power plant. We retrieve XCO₂ using the Iterative Maximum A Posteriori –
 149 Differential Optical Absorption Spectroscopy (IMAP-DOAS) algorithm, as implemented in
 150 Cusworth et al. (2021). This approach estimates XCO₂ by decomposing an observed radiance
 151 spectrum into high and low frequency features between 1900-2100 nm. For high-frequency features,
 152 we simulate atmospheric transmission of CO₂, H₂O, and N₂O using a Beer-Lambert approximation.
 153 For low-frequency features (e.g., surface reflectance, aerosol scattering), we use an 8-degree
 154 polynomial. The forward model that drives IMAP-DOAS therefore has the following form:

$$155 \quad F^h(\mathbf{x}) = I_0(\lambda) \exp \left(- \sum_{n=1}^6 s_n \sum_{l=1}^{72} A_l \tau_{n,l} \right) \sum_{k=0}^K a_k \lambda^k \quad (1)$$

156 Where F^h is simulated backscattered radiance at wavelength λ , I_0 is incident solar intensity, A_l is the
 157 airmass factor at vertical level $l \in [1,72]$, $\tau_{n,l}$ is the optical depth for each trace gas element, s_n is the
 158 scaling factor applied to the optical depth, and a_k is a polynomial coefficient ($K=8$). Optical depths
 159 are computed by querying meteorological information for pressure and temperature from the
 160 MERRA-2 reanalysis (Gelaro et al., 2017), and using that information to select proper HITRAN

161 absorption cross sections for each trace gas (Kochanov et al., 2016). To compare the model from
 162 Equation 1 against PRISMA observed radiance (\mathbf{y}), we compute $F^h(\mathbf{x})$ between 1900-2100 nm at
 163 0.02 nm resolution, then convolve the output using the PRISMA full-width half maximum, and
 164 sample at PRISMA wavelength positions. This results in vector $\mathbf{F}(\mathbf{x})$ that is comparable to \mathbf{y} . The
 165 vector \mathbf{x} , also called the state vector, includes scale factors for CO₂, H₂O, N₂O, and polynomial
 166 coefficients: $\mathbf{x} = (s_{CO_2}, s_{H_2O}, s_{N_2O}, a_0, \dots, a_8)$.

167 XCO₂ is retrieved from PRISMA radiance using a Bayesian optimal estimation approach
 168 (Rodgers, 2000). Here, the optimized state vector solution, or posterior, is solved through Gauss-
 169 Newton iteration:

$$170 \quad \mathbf{x}_{i+1} = \mathbf{x}_A + (\mathbf{K}_i^T \mathbf{S}_0^{-1} \mathbf{K}_i + \mathbf{S}_A^{-1})^{-1} \mathbf{K}_i^T \mathbf{S}_0^{-1} [\mathbf{y} - \mathbf{F}(\mathbf{x}_i) + \mathbf{K}_i(\mathbf{x}_i - \mathbf{x}_A)] \quad (2)$$

171 Where $\mathbf{S}_0 = [\boldsymbol{\epsilon}\boldsymbol{\epsilon}^T]$ is the observation error covariance matrix defined by the instrument signal to noise
 172 ratio (SNR), \mathbf{x}_A is the prior estimate of the state vector, and \mathbf{S}_A is the prior error covariance matrix.
 173 The matrix \mathbf{K} , or Jacobian matrix, represents the first derivative of the $\mathbf{F}(\mathbf{x})$ with respect to the state
 174 vector:

$$175 \quad \mathbf{K}_i = \left. \frac{\partial \mathbf{F}}{\partial \mathbf{x}} \right|_{\mathbf{x}=\mathbf{x}_i} \quad (3)$$

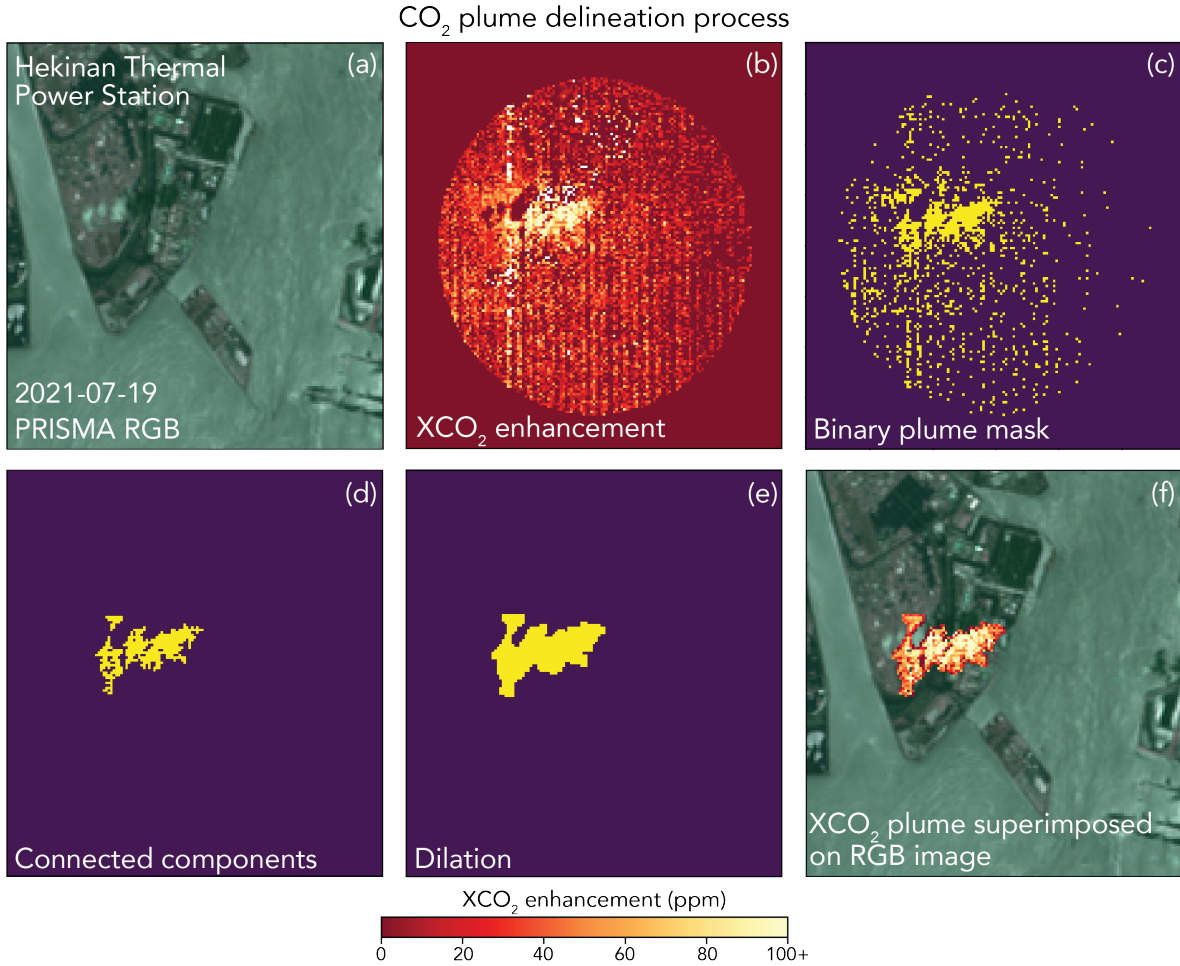
176 The posterior error covariance matrix can be computed explicitly to quantify retrieval precision:

$$177 \quad \hat{\mathbf{S}} = (\mathbf{K}_i^T \mathbf{S}_0^{-1} \mathbf{K}_i + \mathbf{S}_A^{-1})^{-1} \quad (4)$$

178 Across the scenes we acquired with PRISMA, using this retrieval approach, we quantify an
 179 average 3.3 ppm precision for an XCO₂ column. Absolute biases in PRISMA XCO₂ retrievals are
 180 less important for CO₂ plume detection and quantification: systematic retrieval biases are removed
 181 from a scene through the quantification and removal of a local background, as described below. To

182 characterize bias in emission quantification, we compare emission rates derived from PRISMA to
183 stack-level CEMS measurements (Section 3.2).

184 We quantified emissions for each PRISMA plume detection using the Integrated Mass
185 Enhancement (IME) approach (Cusworth et al., 2021). However, we updated the masking scheme
186 for this analysis to produce more reliable masks for each CO₂ plume. Figure 1 shows the plume
187 masking procedure for a plume detected at the Hekinan, Japan power plant on July 19, 2021. First,
188 we apply a background threshold to differentiate candidate plume pixels from the background
189 (method to quantify background threshold described in ~~Results section~~Section 3.2). We then group
190 enhanced XCO₂ pixels into clusters of at least 20 connected pixels. These groups are then buffered
191 with a one-pixel dilation filter to smooth edges and any gaps that exist in a group (Dougherty, 1992).
192 Finally, each cluster is considered part of the plume if at least one of its pixels is within 500 m of an
193 exhaust stack.



194

195 **Figure 1.** Example of the plume delineation and masking process performed on XCO₂ retrievals
 196 derived from PRISMA observations. Panel (a) shows the simultaneously observed RGB PRISMA
 197 imagery, panel (b) shows retrieved XCO₂ above the background, panels (c)-(e) show the plume
 198 masking procedure to isolate enhanced pixels and remove noise, and panel (f) shows the resulting
 199 CO₂ plume superimposed on the RGB imagery.

200

201 IME is calculated for a plume using the following equation:

202

$$\text{IME} = \sum_{i=1}^N \Delta\Omega_i \Lambda_i \quad (5)$$

203 where $\Delta\Omega_i$ is the XCO₂ mass enhancement in pixel i relative to background (kg m⁻²), Λ_i is the pixel
204 area (900 m²), and N is the number of pixels in the plume. The CO₂ emission rate Q is estimated from
205 the IME using the following relationship:

$$206 \quad Q = \frac{U_{eff}}{L} \text{ IME} \quad (6)$$

207 where $L = \sqrt{\sum_{i=1}^N \Lambda_i}$ is the plume length and U_{eff} is the effective wind speed, ~~which accounts for~~
208 ~~turbulent dissipation. The effective wind speed relates IME and plume length parameterizations to~~
209 ~~true emission rates. This relationship can be empirically estimated through large eddy simulations~~
210 ~~using the 10-m wind speed (U_{10}). Here we ~~We estimate~~ apply the U_{eff} from the 10-m wind speed~~
211 ~~(U_{10}) using a relationship derived~~ derived empirical relationship (from Varon et al., 2018):

$$212 \quad U_{eff} = 1.1 \log U_{10} + 0.6. \quad (7)$$

213 where U_{eff} and U_{10} are in units of [m s⁻¹]. We query the ERA5-Land reanalysis using the Open-Meteo
214 Application Programming Interface (open-meteo.com), which provides hourly wind information
215 globally at 0.1° spatial resolution (Muñoz-Sabater et al., 2021). Uncertainty due to winds is calculated
216 by generating an ensemble of U_{10} values assuming 50% error (Cusworth et al., 2021). Uncertainty
217 due to the CO₂ background is calculated by generating many emission estimates and calculating a
218 standard deviation using an ensemble of background thresholds. Background thresholds are set to
219 vary with scene-averaged CO₂ retrieval precision. Total emission uncertainty is estimated by adding
220 in quadrature the contribution of wind and background uncertainties.

221

222 2.3-2 OCO-3 ~~tasking observations~~ and quantification

223 OCO-3 is also a tasked mission: it can take SAMs over any place of interest within the latitude
224 range of the ISS orbit (about 52° S to 52° N). In addition to the SAM locations we supplied to OCO-

225 3 to overlap with PRISMA targets, there are many other power plant and fossil fuel combustion
 226 sources that make up its set of mission targets. However, unlike PRISMA, OCO-3 does not consider
 227 cloud forecasts, snow cover, or viewing geometry when planning SAMs and thus the majority of
 228 observations fail to produce useful maps of XCO₂. Additionally, aerosol- and albedo-induced XCO₂
 229 artifacts are present in many SAMs (Bell et al., 2023) and thus make the detection of plumes even
 230 more difficult.

231 For all cloud-free soundings, OCO-3 XCO₂ concentrations are derived using the
 232 Atmospheric Carbon Observations from Space (ACOS; O’Dell et al., 2012; Crisp et al., 2012; O’Dell
 233 et al., 2018) v10 optimal estimation retrieval, which employs the Levenberg-Marquardt modification
 234 of the Gauss-Newton method. In this work, bias corrected XCO₂ from the OCO-3 Lite files is used
 235 but the official data quality flag is not applied. This was done because often the quality flag removes
 236 XCO₂ retrievals within the plume and makes emission estimation more difficult or impossible
 237 (Nassar et al., 2022). For SAMs where we visually identified CO₂ plumes (e.g., Figure 2), emission
 238 rates are estimated using two approaches: (1) a Gaussian plume model and (2) the IME method. For
 239 the Gaussian plume model approach, we follow the algorithm outlined in Nassar et al. (2022):

$$240 \quad V(x, y) = \frac{Q}{\sqrt{2\pi}\sigma_y(x)u} e^{-\frac{1}{2}\left(\frac{y}{\sigma_y(x)}\right)^2} \quad (8)$$

$$241 \quad \sigma_y(x) = a \cdot \left(\frac{x}{x_o}\right)^{0.894} \quad (9)$$

242 Where V represents the vertical columns within the plume (g/m²), Q is the CO₂ emission rate (g/s),
 243 y is the wind direction perpendicular to the plume (m), u is the wind speed at the height of the plume
 244 at its midline (m/s) assuming plume rise of 250 m above the stack height, $\sigma_y(x)$ is the standard
 245 deviation of the y -direction, x_o is a characteristic plume length (1000 m), and a is a stability
 246 parameter (Nassar et al., 2021). Following Nassar et al. (2022), wind speed and direction inputs are

247 estimated by taking the average of ERA-5 (Bell et al., 2020) and MERRA-2 reanalysis data. The
248 wind direction is optimized by rotating the plume, typically between -30° to 30° away from the mean
249 ERA-5/MERRA-2 direction, and calculating the correlation coefficient (R) of the modeled and
250 observed XCO_2 . The optimized wind direction is the direction that produces the largest R . The
251 background is typically estimated by averaging OCO-3 footprints within a radius of 30 km, excluding
252 the plume itself and a narrow 3 km buffer zone. However, if there are visible artifacts in the XCO_2
253 background that are unrelated to the power plant plume, the background field is modified to avoid
254 them. For example, decreasing the radius of footprints used from 30 km to 20 km. The uncertainty
255 in wind speed is calculated by taking the difference of the emission estimate using two different
256 models (ERA-5 and MERRA2). The background concentration uncertainty is calculated by
257 estimating Q using three different background radii of 30, 40, and 50 km. Q is also calculated for a
258 30 km radius background but only using the left and right halves of the background, relative to the
259 direction of the plume. The standard deviation of both these methods is calculated and the larger of
260 the two is the background uncertainty. The plume rise uncertainty is calculated by estimating Q using
261 plume rise values of 100, 200, 250, 300, and 400 m and taking the standard deviation of those values.
262 Total uncertainty on the emission rate Q using the Gaussian plume method is estimated by adding in
263 quadrature the contribution of wind speed, background concentration, and plume rise uncertainties.

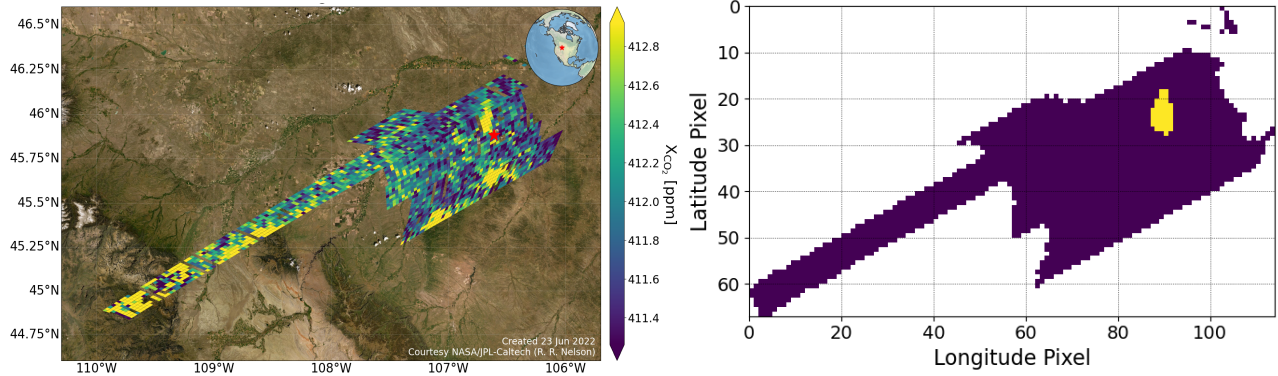
264 To obtain another estimate of emission rate, we also apply an IME quantification approach to
265 the CO_2 plumes, which to our knowledge is the first time the IME method has been applied to OCO-
266 3 SAMS at coal power plants. We first interpolate the XCO_2 retrievals in a SAM to a uniform 2×2
267 km^2 grid to account for occasional OCO-3 footprint overlap. Similar to Varon et al. (2018), 3×3
268 pixel neighborhoods are sampled and the distributions are compared to the background using a
269 Student's t -test. The default confidence level for the t test is 95% but this is often lowered to visually

270 capture most of the plume. The plume is then smoothed using a 3×3 pixel median filter and a
271 Gaussian filter with a standard deviation of 0.5. The U_{eff} calculation is done using an equation
272 approximately equal to Equation 7 ($U_{eff} = 1.0 \log U_{10} + 0.55$). Other recent studies have used various
273 methods (Lin et al., 2023; Brunner et al., 2023), but further research is needed to determine the most
274 accurate way to estimate U_{eff} for an OCO-3-like instrument. The wind direction is the optimized
275 direction determined by the Gaussian plume model. The background XCO₂ estimate is taken from
276 the Gaussian plume model methodology and the plume is typically required to be within 50 km
277 downwind and 8 km crosswind of the source, although these parameters are modified if the plume
278 curves outside of the 8 km crosswind threshold or there are XCO₂ artifacts that should be avoided.

279 The uncertainty for the IME method is estimated similarly to the Gaussian plume model
280 method. The uncertainty in wind speed is calculated by taking the standard deviation of the emission
281 estimates using wind speed from two different models (ERA-5 and MERRA2). The background
282 concentration uncertainty is calculated by estimating Q using the different backgrounds calculated in
283 the Gaussian plume model method: a 20 km radius, 30 km radius, 40 km radius, left half, full circle,
284 and right half. The standard deviation of the three radii estimates and left half, full circle, and right
285 half estimates are calculated and the larger of the two is the background uncertainty. Uncertainty of
286 the Student's t -test confidence level is also estimated. The confidence level and -10% and +10% of
287 the confidence level are used to find Q . For example, if the confidence level needed to visually
288 capture the XCO₂ plume is 85%, Q is calculated for 75%, 85%, and 95% and the standard deviation
289 of those three values represents the confidence level uncertainty. Total uncertainty on the emission
290 rate Q using the IME method is estimated by adding in quadrature the contribution of wind speed,
291 background concentration, and Student's t -test confidence level uncertainties.

292 Figure 2 shows IME methodology successfully identifying an XCO₂ plume from an OCO-3
293 SAM taken over the Colstrip power plant.

294



295

296 **Figure 2.** IME plume identification approach applied to an example OCO-3 SAM at the Colstrip
297 power plant on 18 August 2021. Left panel: OCO-3 SAM bias corrected XCO₂. Right panel: yellow
298 pixels indicate the final plume mask.

299

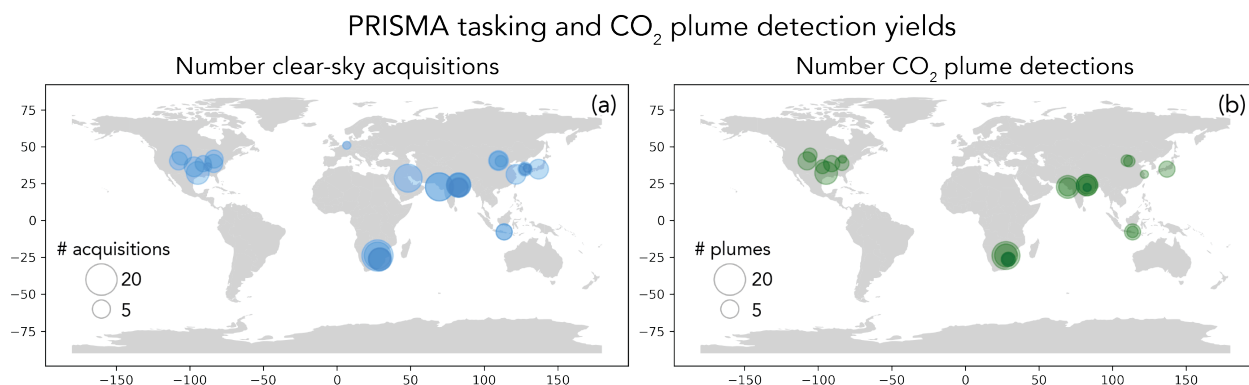
300 **3 Results**

301 *3.1 Global yields from two years of ~~tasking~~ observations*

302 Figure 3a shows a global map of power plants we targeted with PRISMA, with the marker
303 for each power plant's location (latitude, longitude) scaled to represent the number of successful
304 acquisitions between 2021-2022. In total, we acquired 181 PRISMA images, which corresponds to
305 314 unique power plant observation scenes. Of these scenes, 210 were of sufficient quality to attempt
306 CO₂ retrieval and plume detection, with quality mostly determined by visual inspection for clouds
307 and haze. Of these 210 scenes, 104 were determined to have CO₂ plumes (Figure 3b). Scenes were
308 marked as containing CO₂ plumes through inspection of XCO₂ and visible imagery: if a large cluster
309 of pixels with elevated XCO₂ above the background were also in the vicinity of a power plant exhaust

310 stack, an analyst would mark the scene as containing a CO₂ plume. ~~Tasking~~Routine tasking
311 observations with PRISMA resulted in an average of 6 acquisitions for each power plant (maximum
312 15), roughly one image acquired per quarter. Of these acquisitions, plumes were detected on average
313 four times per facility (maximum 12).

314 For OCO-3, 1363 power plant SAMs were taken during September 2019 to December 2022.
315 Of these, 139 XCO₂ plumes emanating from power plants were visually identified. However, only
316 14 were for power plants that were also ~~tasked-observed~~ by PRISMA and have CEMS validation
317 (nine Colstrip cases, two Martin Lake cases, and three Craig cases). The acquisition rates are low
318 relative to PRISMA because OCO-3 does not account for scene favorability when planning its SAMs.
319 For example, OCO-3 took 66 Colstrip SAMs from 2019-2022 yet only yielded nine high-quality
320 XCO₂ plume cases.

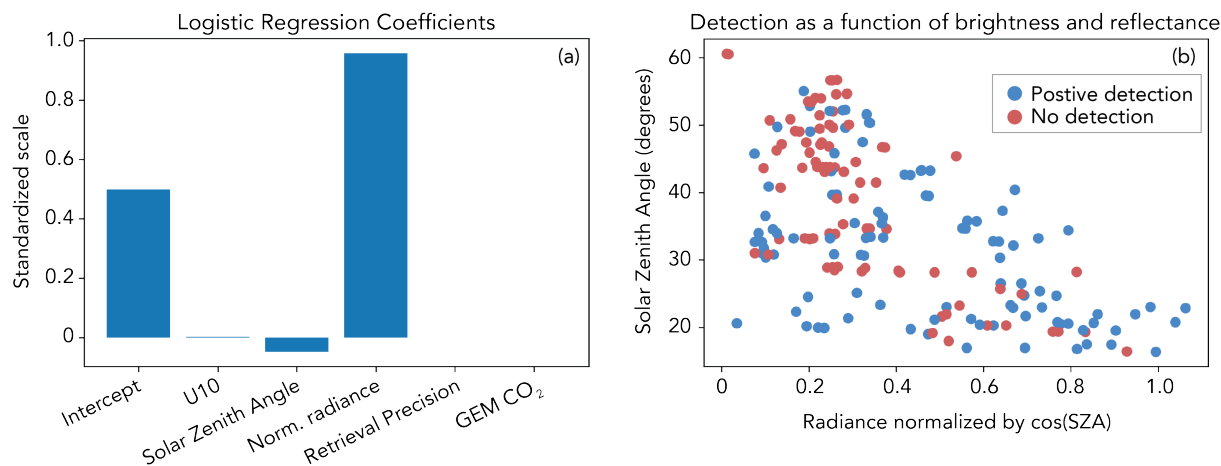


321
322 **Figure 3.** Data yields from ~~tasking~~ PRISMA continually between 2021-2022. Panel (a) shows the
323 number of clear-sky acquisitions for each power plant. Panel (b) shows the number of plumes
324 detected by an analyst for each of the ~~tasked-observed~~ power plants.

326 The low observed average detection rate of plumes for PRISMA (50%) CO₂ plumes is a result
327 of three primary factors: (1) observing conditions at each facility including solar zenith angle (SZA)

328 and surface reflectance; (2) local meteorology; and (3) operational status at each power plant at the
329 time of acquisition. To test how well these factors predict the presence of a plume [for PRISMA](#), we
330 fit a logistic regression classification function with a sparse (L1) penalty to our dataset (Fan et al.,
331 2008). This algorithm fits a logit function to the plume detection outcome of each scenes (i.e.,
332 detected plume = TRUE, no detected plume = FALSE) using a set of predictor variables that are
333 likely candidates to explain prediction results. In this setup, the statistical model is fit using the
334 following predictor variables – SZA, U_{10} , average single-sounding retrieval precision across the
335 scene, annual bottom-up emission estimate for the power plant using GEM, and average observed
336 radiance between 1900-2100 nm within the scene normalized by the cosine of the SZA. This last
337 factor is a simple proxy for surface reflectance, although it does not take into account other factors
338 that influence radiance observations (e.g., water vapor, aerosols, other atmospheric constituents). We
339 split the data so that 50% was used to train the model and 50% was reserved as a test set. The predictor
340 variables were all standardized by their mean and standard deviation before the model was fit. The
341 results of classification can be summarized using two statistics: precision (ratio of true positives to
342 sum of true positives and false positives) and recall (ratio of true positives to sum of true positives
343 and false negatives). The results of fitting a logistic regression model to the data show minor
344 prediction performance, with precision = 0.60 and recall = 0.69 for positive plume detection. The
345 regression coefficients are shown in Figure 4a. The coefficient with the highest weight is normalized
346 radiance. Figure 4b shows SZA against normalized radiance, with red dots indicating no plume
347 detection and blue dots representing positive plume detection. Though no clear separation exists,
348 there is a cluster of no plume detection at high SZA and low normalized radiance. This is a consistent
349 and expected relationship, as SZA and surface reflectance are principal drivers of the quantity of light
350 that is observed by the satellite, and therefore SNR of the observation.

351



352

353 **Figure 4.** CO₂ plume prediction using various atmospheric, retrieval, and bottom-up information.

354 Panel (a) shows the results of fitting a logistic regression classification model to the set of PRISMA

355 acquisitions where an analyst identified the presence or lack of a plume. Panel (b) shows the top two

356 explanatory variables (SZA and normalized radiance) along with plume classification.

357

358 The logistic regression model performed better on the test data set than predictions made at

359 random, though the prediction performance was still low. Missing from the model is sub-annually

360 resolved information regarding operating status. For most of the power plants outside the U.S., we

361 do not have information on daily operations of a power plant. In many cases of non-detects, we could

362 simply be observing a power plant temporarily not in operation. Another possibility is that at the time

363 of acquisition, some power plants were operating at reduced capacity, meaning that CO₂ emission

364 rates were lower than those predicted by annual emission factors or activity data. If the true CO₂

365 emission rate was below the minimum detection limit (MDL) possible by the PRISMA satellite, then

366 it would show as a non-detect. However, even if the emission were near or slightly above the

367 PRISMA MDL, the probability of detection would still be low as slight variations in atmospheric
368 properties, as seen in Figure 4, would then influence the ability to detection a CO₂ plume.

369

370 *3.2 Validation of PRISMA and OCO-3 emission rates against CEMS*

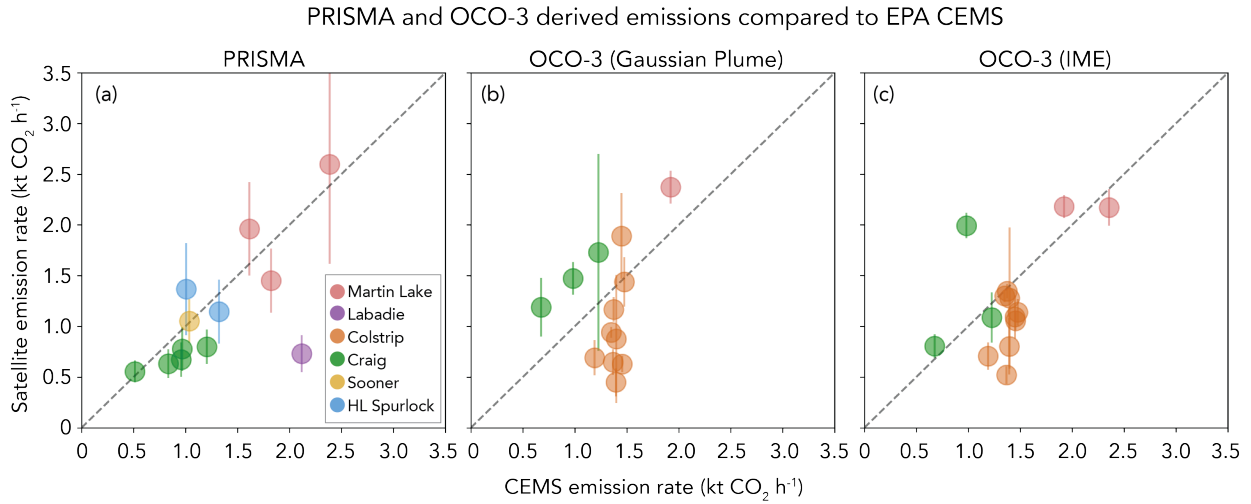
371 For each power plant where a CO₂ plume was identified, we quantify emissions using the
372 IME approach described by Equations 5-7. In order to estimate the XCO₂ mass enhancement ($\Delta\Omega$ in
373 Equation 1), a local background must be quantified and subtracted from total XCO₂ retrievals across
374 the scene. To do this, we apply a concentration threshold β to initiate the plume masking and
375 segmentation process (described in Methods section). Once we have a plume mask, we apply another
376 concentration threshold γ to the remaining XCO₂ pixels that exist outside of the plume. This value γ
377 represents the XCO₂ background that we use to calculate the XCO₂ enhancement that is used in the
378 IME formulation of Equation 1. Thresholds β and γ largely influence the magnitude of the emission
379 rate and are not known a priori. For global generalizability, we wish to estimate β and γ such that
380 they do not vary across power plants, seasons, regions, etc. Therefore, we parameterize β and γ as
381 percentiles under the assumption that the local contrast between enhanced CO₂ plume pixels and the
382 background should be similar across PRISMA scenes.

383 To estimate values for β and γ , we compare EPA CEMS data for power plants in the U.S.
384 with estimated emission rates from PRISMA. In total, we have 12 scenes in the U.S. with CEMS
385 information that pertain to 5 power plants. We then optimize β and γ such that the output of an
386 ordinary least squares regression produces a slope near unity. Figure 5a shows the results of this
387 optimization which produces an optimal β percentile of 94% and a γ percentile of 62%. The results
388 also show decent correlation between CEMS data and PRISMA-derived emission rates ($R^2 = 0.43$).
389 A single outlier at the Labadie power plant (imaged July 10, 2022) shows the largest discrepancy

390 from CEMS data (69%), but the remaining plumes show average 27% relative difference from CEMS
391 data. If we remove the one data point at Labadie, the R^2 improves to 0.75. Though a limited sample
392 size, between PRISMA and OCO-3, these scenes represent variability in solar geometries (20-40°
393 SZA), surface reflectance (0.09-0.90 normalized radiance), and reported emission rates (0.51 – 2.39
394 kt CO₂ h⁻¹). Therefore, we use these optimal parameters and apply them to our global dataset of
395 PRISMA detections. These emission rates are reported in Table 1. There are some instances when
396 performing IME emission calculations using these thresholds and plume masking technique do not
397 result in emission rates (e.g., the plume masking procedure produces a mask with no pixels). In these
398 cases, we report a detection but not an emission quantification.

399 Figures 5b and 5c shows the comparison between OCO-3 and CEMS at some power plants
400 that overlap with PRISMA ~~tasking observations~~ (14 scenes total). OCO-3 Gaussian plume model
401 emission rates (Fig. 5b) have an improved correlation compared to PRISMA ($R^2 = 0.51$), although
402 with greater bias (average 47% relative difference from CEMS). The OCO-3 IME estimates (Fig.
403 5c) have worse R^2 (0.32) but a better RMSE (0.45 kt CO₂/hr) compared to the Gaussian plume model
404 estimates (0.84 kt CO₂/hr), with 9 of the 14 cases being within 30% of the reported CEMS emission
405 and an average relative difference of 30% for all 14 cases. Additionally, the least squares fit for IME
406 is closer to the 1-to-1 line than for the Gaussian plume model.

407



408

409 **Figure 5.** Comparison of emission rates in the U.S. between satellite-derived estimates and CEMS
 410 information. Panel (a) shows a comparison between PRISMA derived emission rates and CEMS (R^2
 411 = 0.43), panel (b) shows a comparison between OCO-3 and CEMS using the Gaussian plume model
 412 ($R^2 = 0.51$), and panel (c) shows a comparison between OCO-3 and CEMS using IME ($R^2 = 0.32$).

413

414 Unique sources of error for OCO-3 emission estimates include geolocation errors in the
 415 XCO₂ product. These errors are typically less than 1 km, but can be up to 2 km (Taylor et al., 2023).
 416 Errors of this magnitude, about the size of an OCO-3 footprint ($\sim 2 \times 2$ km²), may mean that an entire
 417 footprint is not included when estimating emissions using the Gaussian plume method, which
 418 assumes that the plume only extends downwind of the known source location. The Gaussian plume
 419 model is also susceptible to wind direction errors, and requires the plume to be Gaussian in shape,
 420 which is often not true. IME, while not suffering from wind direction or geolocation-induced errors,
 421 assumes that the entire plume is captured in a given SAM, which is sometimes not true and results in
 422 an underestimation of emissions. IME is also sensitive to errors in U_{eff} parameterization.

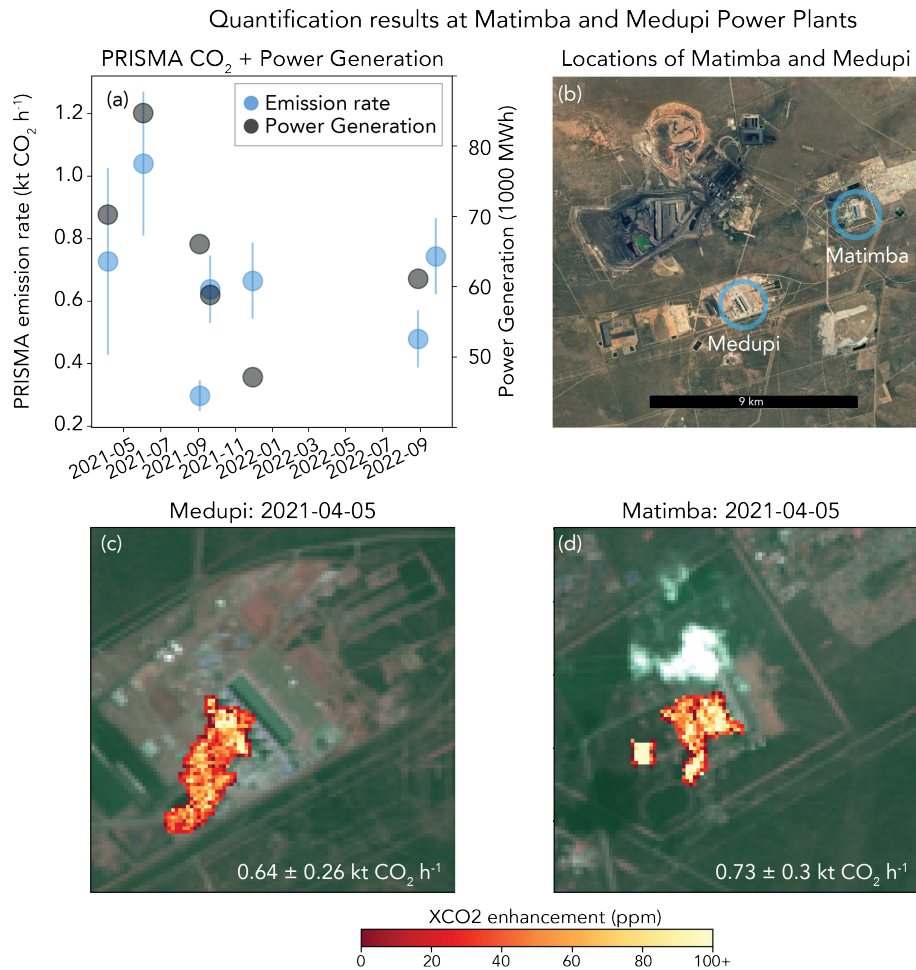
423

424 3.3 Comparison and fusion of PRISMA and OCO

425 Outside the U.S., PRISMA observed the Matimba power station in South Africa 11 times and
426 quantified emission rates 7 times. Emissions from Matimba have previously been quantified and
427 validated using OCO-2 (Hakkarainen et al., 2021). This station does not report hourly emission rates,
428 but does report daily power generation (Eskom, 2023). Though not a direct comparison, we can use
429 this information to check if the emission quantification approach we describe above captures some
430 variability in activity at this power plant. Figure 6a shows the emission rates we quantified compared
431 against reported power generation. We see rough agreement in variability – the high power
432 generation reported between Apr to July 2021 (70000-85000 MWh) drop for subsequent dates
433 (47000-66000 MWh) between Sep 2021 to Sep 2022, a drop which is also seen in the PRISMA-
434 derived CO₂ emission rate. Across all observations, we estimate an emission rate range of 0.30-1.04
435 kt CO₂ h⁻¹ (average 0.66 kt CO₂ h⁻¹). This average emission rate is substantially lower than the
436 average 2.50 kt CO₂ h⁻¹ emission rate estimated from OCO-2 and TROPOMI between 2018-2020,
437 but within the range of emissions estimates directly quantified with OCO-2 (0.30-7.20 kt CO₂ h⁻¹;
438 Hakkarainen et al., 2021). However, this discrepancy could be result of (1) changes in activity or
439 variability or (2) existence of other nearby emission sources. For changes in activity, during August
440 2020, the Matimba reported a large range of power generation (65000-94000 MWh) and emission
441 estimates derived directly from OCO-2 were also highly variable (0.88-4.33 kt CO₂ h⁻¹). Given that
442 maximum power generation at the time of a PRISMA observation was 85000 MWh, some of the
443 discrepancy in maximum CO₂ quantification between PRISMA and OCO-2 could be due to activity.

444 Nearby (7 km) the Matimba Power Station is the Medupi Power Plant (Figure 6b). Figure 6c
445 show the Medupi CO₂ plume observed during the same PRISMA overpass on Apr 5, 2021. The
446 PRISMA derived emission rate for Medupi is 0.64 ± 0.26 kt CO₂ h⁻¹ and for Matimba is 0.73 ± 0.30

447 kt CO₂ h⁻¹. Given the proximity of the two power plants, the higher derived emission rate reported
 448 for Matimba from previous studies could actually be a result of a net emission from these two
 449 facilities. The OCO-2 flight track is located tens of kilometers downwind from Matimba and Medupi,
 450 making a clear delineation between potentially co-emitted distinct emission plumes near impossible.
 451 If we sum emission rates from both Medupi and Matimba, we quantify a range of 0.89-1.73 kt CO₂
 452 h⁻¹ (1.30 ± 0.28 kt CO₂ h⁻¹), which is still lower, but closer to the average emissions quantified by
 453 OCO-2.



454
 455 **Figure 6.** Emission rates and reported power generation at the Matimba and Medupi power plants in
 456 South Africa. Panel (a) shows the CO₂ emission rates derived from PRISMA and the reported daily

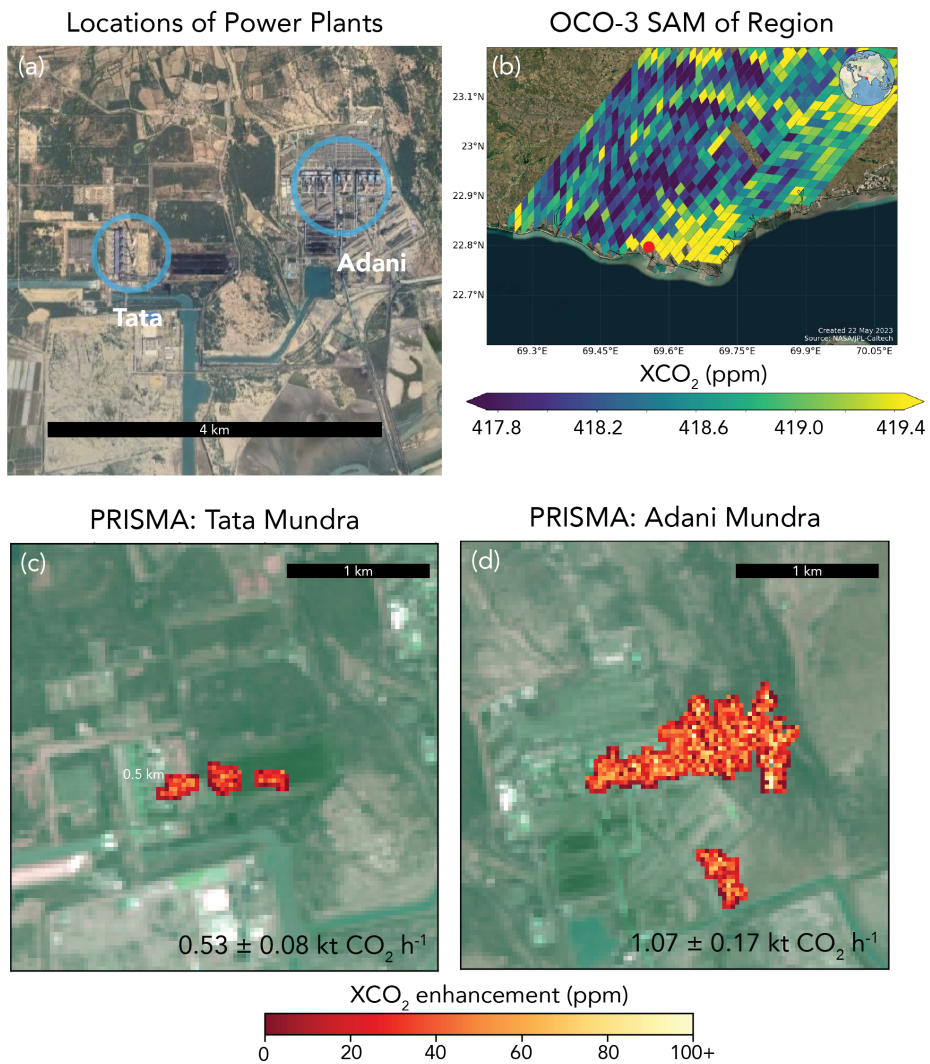
457 power generation for the day of PRISMA overpass. Panel (b) shows the locations of the Medupi and
458 Matimba power plants (base imagery provided by Google Earth; © Google Earth 2023). Panels (c)
459 and (d) show plume imagery and emission rates for a PRISMA overpass on Apr 5, 2021.

460

461 The ability to differentiate the contribution of unique point sources to a regional total is an
462 application made possible by joint observing of imaging spectrometers and atmospheric sounders.
463 Figure 7 shows observations that were made at the Tata Mundra Ultra Mega Power Plant and the
464 Adani Mundra Thermal Power Project: two power plants less than 3 km apart. Both OCO-3 and
465 PRISMA imaged the power plants on Apr 9, 2022. Figure 7b shows the OCO-3 SAM (taken 04:41
466 UTC) – large CO₂ enhancements appear along the coastline likely associated with emission from
467 these power plants. PRISMA imaged the power plants less than two hours later (06:02 UTC) and
468 detected CO₂ plumes at each facility (Figure 7b-c). The OCO-3 derived emission rate using Gaussian
469 plume approaches is 5.5 ± 0.7 kt CO₂ h⁻¹, but the emission rate derived using the IME approach is
470 much lower (3.0 kt CO₂ h⁻¹). For this case, the IME approach may be more appropriate as the shape
471 of the OCO-3 plume (Figure 7b) is more diffuse in nature and does not visibly resemble a Gaussian
472 structure. The PRISMA emission rate for the Adani plant is 1.07 ± 0.17 kt CO₂ h⁻¹ and for the Adani
473 Tata Mundra plant is 0.53 ± 0.08 kt CO₂ h⁻¹. We can use this information to estimate that 67% of the
474 net CO₂ emission came from Adani, and the remaining 33% came from the Tata plant. The combined
475 emission rate (1.60 ± 0.25 kt CO₂ h⁻¹) is lower than the OCO-3 IME emission rate. Like the Matimba
476 power plant, some of this discrepancy is likely may partially be explained by bias or uncertainty in
477 retrievals, background, and wind information. Also, lower estimates of CO₂ emissions from PRISMA
478 are consistent with the fact that PRISMA is only sensitive to emissions at two exhaust stacks, while
479 the OCO-3 observation includes all CO₂ sources in the industrial area around Mundra.– Continued

480 validation of retrieved emission rates against ground standards (e.g., CEMS) will help ~~reduce this~~
 481 better quantify bias and uncertainty. However, even with ~~this~~-lingering uncertainty, the near
 482 simultaneous observations of OCO-3 and PRISMA can help us disentangle the relative contributions
 483 from each power plant.
 484

Near-simultaneous OCO-3 & PRISMA observations (2022-04-09)



485
 486 **Figure 7.** Near-simultaneous observation of two power plants in Mundra, India on Apr 9, 2022. Panel
 487 (a) shows the locations of two power plants spaced less than 3 km apart: Tata Mundra and Adani

488 Mundra Power Stations (base imagery provided by Google Earth; © Google Earth 2023). Panel (b)
489 shows the OCO-3 SAM with a red dot showing the location of the power plants. Panel (c) and (d)
490 show the PRISMA acquisition (less than 2 hours after OCO-3) over the two power plants with
491 associated emission rates.

492

493 **Conclusion**

494 We ~~tasked~~observed a global set of power plants for two years between 2021-2022 with both
495 PRISMA and OCO-3 to test the ability of these satellite platforms to do routine operational
496 monitoring of CO₂ emissions. When PRISMA observations were of sufficient quality to perform
497 XCO₂ retrievals, we detected CO₂ plumes nearly half of the time. We fit a logistic regression
498 classification using plume detections and find that there is some relationship between SZA and
499 surface reflectance that partially explains plume prediction; consistent given that these factors are
500 major drivers of SNR. The remaining non-plume detections may be due to operational status of a
501 power plant at the time of observation. We compared emission rates from both PRISMA and OCO-
502 3 to power plants in the U.S. where we have access to hourly *in situ* CEMS emission information.
503 We find significant correlation between satellite and *in situ* estimates, though some significant biases
504 may exist for some of the observations for both PRISMA and OCO-3. Also, the quantity of CEMS
505 observations was limited (~10 for each instrument), so robust calibration is not yet possible. Still,
506 early results show that under the right conditions, satellites can provide reliable estimates of CO₂
507 emissions at discrete point source locations. This is consistent with the close agreement between
508 airborne imaging spectrometer emissions and CEMS information (Cusworth et al., 2021).

509 Fusion of information from atmospheric sounders like OCO-3 and imaging spectrometers
510 like PRISMA is valuable for cross-validation and source attribution. We see this particularly for our

511 examples at the Matimba and Medupi power plants in South Africa and the Tata and Adani power
512 plants in Mundra, India. In these cases, and particularly at Mundra where near-simultaneous
513 PRISMA and OCO-3 observations were taken, OCO-2/3 provides a local, but coarse resolution
514 emission constraint for a complex of facilities that emit large CO₂ quantities. PRISMA, with its 30
515 m pixel resolution, then can help refine relative contributions of single emitters against the net
516 emission flux. More work is needed to refine cross-validation between instruments, but initial
517 observationasking shows one avenue for data from multiple observing systems to be complementary
518 aggregated and analyzed.

519 Even when combining information from both satellites, there is still too little sampling to
520 constrain facility emissions within low uncertainties. Cusworth et al. (2021), using arguments from
521 Hill and Nassar (2019), suggested that nearly 30 unbiased observations from a PRISMA-class
522 instrument is needed per year at each power plant to reduce annual uncertainties below 14% (i.e.,
523 reduce emission uncertainty from Non-Annex I countries below 1 Gt CO₂ per year). No power plant
524 in this study met this minimum sampling requirement. However, there will be a significant increase
525 in data volumes and observation performance of satellite remote sensing capabilities for CO₂, from
526 both recently launched and planned imaging spectrometers including EMIT (launched 2022; Thorpe
527 et al., in revision); EnMAP (launched 2022; Guanter et al., 2015); Carbon Mapper/Tanager 1-2
528 (Planned launch 2024; Duren et al., 2021), and atmospheric sounders including CO₂M (Sierk et al.,
529 2019). Improved observation of global power plants and emission quantification with robust error
530 characterization will be vital to reduce global uncertainty of anthropogenic emissions from fossil fuel
531 combustion sources.

532

533 **Data Availability.**

534 The OCO-3 XCO₂ and other retrieval properties are publicly available at the NASA Goddard Earth
535 Science Data and Information Services Center (GES-DISC). The full suite of retrieval products in
536 the standard per-orbit format can be obtained at OCO Science Team et al., 2021,
537 <https://doi.org/10.5067/D9S8ZCHCADE>. The lightweight per-day format data (Lite files), which
538 includes the bias corrected estimates of XCO₂, can be obtained at OCO Science Team et al., 2022,
539 <https://doi.org/10.5067/970BCC4DHH24>. PRISMA data including radiance for each scene and
540 XCO₂ retrievals is available at <https://doi.org/10.5281/zenodo.8083596>.

541

542 **Acknowledgments.** This work was supported by the Orbiting Carbon Observatory Science Team.
543 We thank the Italian Space Agency for the PRISMA satellite targets. Portions of this work were
544 undertaken at the Jet Propulsion Laboratory, California Institute of Technology, under contract with
545 NASA.

546

547 **Author Contributions.** DHC designed the study. DHC, AKA, RJ tasked and acquired PRISMA
548 data. DHC performed PRISMA emission quantification and validation. RRN performed OCO-3
549 quantification and validation. RN and JPM helped implement OCO-3 quantification algorithms. All
550 authors provided feedback on results and the manuscript.

551

552

553 **Competing interests.** The authors declare no conflicts of interest.

554

555 **References**

556 Beirle, S., Borger, C., Dörner, S., Eskes, H., Kumar, V., de Laat, A. and Wagner, T., 2021. Catalog
557 of NO_x emissions from point sources as derived from the divergence of the NO₂ flux for
558 TROPOMI. *Earth System Science Data*, 13(6), pp.2995-3012. DOI [https://doi.org/10.5194/essd-13-](https://doi.org/10.5194/essd-13-2995-2021)
559 [2995-2021](https://doi.org/10.5194/essd-13-2995-2021)

560
561 Bell, B., Hersbach, H., Berrisford, P., Dahlgren, P., Horányi, A., Sabater, M., et al.
562 (2020). ERA5 hourly data on pressure levels from 1950 to 1978 (preliminary
563 version). Copernic. Clim. Change Serv. (C3S) Clim. Data Store (CDS). AvailableAt:
564 [https://cds.climate.copernicus-climate.eu/cdsapp#!/dataset/reanalysis-era5-](https://cds.climate.copernicus-climate.eu/cdsapp#!/dataset/reanalysis-era5-pressure-levels-preliminary-back-extension?tab=overview)
565 [pressure-levels-preliminary-back-extension?tab=overview.](https://cds.climate.copernicus-climate.eu/cdsapp#!/dataset/reanalysis-era5-pressure-levels-preliminary-back-extension?tab=overview)

566
567 Bell, E., O'Dell, C.W., Taylor, T.E., Merrelli, A., Nelson, R.R., Kiel, M., Eldering, A., Rosenberg,
568 R. and Fisher, B., 2023. Exploring bias in the OCO-3 snapshot area mapping mode via geometry,
569 surface, and aerosol effects. *Atmospheric Measurement Techniques*, 16(1), pp.109-133. DOI
570 <https://doi.org/10.5194/amt-16-109-2023>

571
572 Brunner, D., Kuhlmann, G., Henne, S., Koene, E., Kern, B., Wolff, S., Voigt, C., Jöckel, P.,
573 Kiemle, C., Roiger, A. and Fiehn, A., 2023. Evaluation of simulated CO₂ power plant plumes
574 from six high-resolution atmospheric transport models. *Atmospheric Chemistry and Physics*, 23(4),
575 pp.2699-2728. DOI <https://doi.org/10.5194/acp-23-2699-2023>

576
577 [Crippa, M., Guizzardi, D., Banja, M., Solazzo, E., Muntean, M., Schaaf, E., Pagani, F., Monforti-](#)
578 [Ferrario, F., Olivier, J., Quadrelli, R., Risquez Martin, A., Taghavi-Moharamli, P., Grassi, G.,](#)

579 Rossi, S., Jacome Felix Oom, D., Branco, A., San-Miguel-Ayanz, J. and Vignati, E., CO2
580 emissions of all world countries - 2022 Report, EUR 31182 EN, Publications Office of the
581 European Union, Luxembourg, 2022, doi:10.2760/730164, JRC130363~~Crippa, M., Oreggioni, G.,~~
582 ~~Guizzardi, D., Muntean, M., Schaaf, E., Lo Vullo, E., Solazzo, E., Monforti-Ferrario, F., Olivier,~~
583 ~~J.G. and Vignati, E., 2019. Fossil CO2 and GHG emissions of all world countries. Publication~~
584 ~~Office of the European Union: Luxemburg.~~

585

586 Crisp, D., Fisher, B.M., O'Dell, C., Frankenberg, C., Basilio, R., Bösch, H., Brown, L.R., Castano,
587 R., Connor, B., Deutscher, N.M. and Eldering, A., 2012. The ACOS CO-2 retrieval algorithm—part
588 II: global X-CO-2 data characterization. *Atmospheric Measurement Techniques*, 5(4), pp.687-707.
589 DOI <https://doi.org/10.5194/amt-5-687-2012>

590

591 Cusworth, D.H., Duren, R.M., Thorpe, A.K., Eastwood, M.L., Green, R.O., Dennison, P.E.,
592 Frankenberg, C., Heckler, J.W., Asner, G.P. and Miller, C.E., 2021. Quantifying global power plant
593 carbon dioxide emissions with imaging spectroscopy. *AGU Advances*, 2(2), p.e2020AV000350.
594 DOI <https://doi.org/10.1029/2020AV000350>

595

596 Dougherty, E.R., 1992. An introduction to morphological image processing. In *SPIE. Optical*
597 Engineering Press.

598

599 Duren, R., Cusworth, D., Ayasse, A., Herner, J., Thorpe, A., Falk, M., Heckler, J., Guido, J.,
600 Giuliano, P., Chapman, J. and Green, R., 2021, December. Carbon Mapper: on-orbit performance
601 predictions and airborne prototyping. In *AGU Fall Meeting Abstracts* (Vol. 2021, pp. A53F-05).

602

603 Elderling, A., Taylor, T.E., O'Dell, C.W. and Pavlick, R., 2019. The OCO-3 mission: measurement
604 objectives and expected performance based on 1 year of simulated data. *Atmospheric Measurement*
605 *Techniques*, 12(4), pp.2341-2370. [DOI https://doi.org/10.5194/amt-12-2341-2019](https://doi.org/10.5194/amt-12-2341-2019)

606

607 Fan, R.E., Chang, K.W., Hsieh, C.J., Wang, X.R. and Lin, C.J., 2008. LIBLINEAR: A library for
608 large linear classification. *the Journal of machine Learning research*, 9, pp.1871-1874. [DOI](https://doi.org/10.5555/1390681.1442794)
609 <https://doi.org/10.5555/1390681.1442794>

610

611 Gelaro, R., McCarty, W., Suárez, M.J., Todling, R., Molod, A., Takacs, L., Randles, C.A.,
612 Darmenov, A., Bosilovich, M.G., Reichle, R. and Wargan, K., 2017. The modern-era retrospective
613 analysis for research and applications, version 2 (MERRA-2). *Journal of climate*, 30(14), pp.5419-
614 5454. <https://doi.org/10.1175/JCLI-D-16-0758.1>

615

616 GEM, Global Energy Monitor's Global Coal Plant Tracker, URL
617 <https://globalenergymonitor.org/projects/global-coal-plant-tracker/tracker/>, last accessed May 24,
618 2023

619

620 Guan, D., Liu, Z., Geng, Y., Lindner, S. and Hubacek, K., 2012. The gigatonne gap in China's
621 carbon dioxide inventories. *Nature Climate Change*, 2(9), pp.672-675. [DOI](https://doi.org/10.1038/nclimate1560)
622 <https://doi.org/10.1038/nclimate1560>

623

624 Guanter, L., Kaufmann, H., Segl, K., Foerster, S., Rogass, C., Chabrillat, S., Kuester, T., Hollstein,
625 A., Rossner, G., Chlebek, C. and Straif, C., 2015. The EnMAP spaceborne imaging spectroscopy
626 mission for earth observation. *Remote Sensing*, 7(7), pp.8830-8857. [DOI](https://doi.org/10.3390/rs70708830)
627 <https://doi.org/10.3390/rs70708830>
628

629 Guo, W., Shi, Y., Liu, Y. and Su, M., 2023. CO2 emissions retrieval from coal-fired power plants
630 based on OCO-2/3 satellite observations and a Gaussian plume model. *Journal of Cleaner*
631 *Production*, 397, p.136525. [DOI https://doi.org/10.1016/j.jclepro.2023.136525](https://doi.org/10.1016/j.jclepro.2023.136525)
632

633 Hakkarainen, J., Szeląg, M.E., Ialongo, I., Retscher, C., Oda, T. and Crisp, D., 2021. Analyzing
634 nitrogen oxides to carbon dioxide emission ratios from space: A case study of Matimba Power
635 Station in South Africa. *Atmospheric Environment: X*, 10, p.100110. [DOI](https://doi.org/10.1016/j.aeaoa.2021.100110)
636 <https://doi.org/10.1016/j.aeaoa.2021.100110>
637

638 Hill, T. and Nassar, R., 2019. Pixel size and revisit rate requirements for monitoring power plant
639 CO2 emissions from space. *Remote Sensing*, 11(13), p.1608. [DOI](https://doi.org/10.3390/rs11131608)
640 <https://doi.org/10.3390/rs11131608>
641

642 Hong, C., Zhang, Q., He, K., Guan, D., Li, M., Liu, F. and Zheng, B., 2017. Variations of China's
643 emission estimates: response to uncertainties in energy statistics. *Atmospheric Chemistry and*
644 *Physics*, 17(2), pp.1227-1239. [DOI https://doi.org/10.5194/acp-17-1227-2017](https://doi.org/10.5194/acp-17-1227-2017)
645

646 IPCC, 2021: *Climate Change 2021: The Physical Science Basis. Contribution of Working Group I*
647 *to the Sixth Assessment Report of the Intergovernmental Panel on Climate Change*[Masson-
648 Delmotte, V., P. Zhai, A. Pirani, S.L. Connors, C. Péan, S. Berger, N. Caud, Y. Chen, L. Goldfarb,
649 M.I. Gomis, M. Huang, K. Leitzell, E. Lonnoy, J.B.R. Matthews, T.K. Maycock, T. Waterfield, O.
650 Yelekçi, R. Yu, and B. Zhou (eds.)]. Cambridge University Press, Cambridge, United Kingdom and
651 New York, NY, USA, In press, doi:[10.1017/9781009157896](https://doi.org/10.1017/9781009157896).

652
653 J. Muñoz-Sabater, Dutra, E., Agustí-Panareda, A., Albergel, C., Arduini, G., Balsamo, G.,
654 Boussetta, S., Choulga, M., Harrigan, S., Hersbach, H., Martens, B., Miralles, D. G., Piles, M.,
655 Rodríguez-Fernández, N. J., Zsoter, E., Buontempo, C., and Thépaut, J.-N.: ERA5-Land: A state-
656 of-the-art global reanalysis dataset for land applications, *Earth Syst. Sci. Data*,13, 4349–4383,
657 2021. <https://doi.org/10.5194/essd-13-4349-2021>.

658
659 Kochanov, R.V., Gordon, I.E., Rothman, L.S., Weisło, P., Hill, C. and Wilzewski, J.S., 2016.
660 HITRAN Application Programming Interface (HAPI): A comprehensive approach to working with
661 spectroscopic data. *Journal of Quantitative Spectroscopy and Radiative Transfer*, 177, pp.15-30.
662 DOI <https://doi.org/10.1016/j.jqsrt.2016.03.005>

663
664 Lin, X., van der A, R., de Laat, J., Eskes, H., Chevallier, F., Ciais, P., Deng, Z., Geng, Y., Song, X.,
665 Ni, X. and Huo, D., 2023. Monitoring and quantifying CO-2 emissions of isolated power plants
666 from space. *EGUsphere*, pp.1-20. DOI <https://doi.org/10.5194/egusphere-2022-1490>

667

668 Loizzo, R., Guarini, R., Longo, F., Scopa, T., Formaro, R., Facchinetti, C. and Varacalli, G., 2018,
669 July. PRISMA: The Italian hyperspectral mission. In *IGARSS 2018-2018 IEEE International*
670 *Geoscience and Remote Sensing Symposium* (pp. 175-178). IEEE. DOI [https://doi.org/](https://doi.org/10.1109/IGARSS.2018.8518512)
671 [10.1109/IGARSS.2018.8518512](https://doi.org/10.1109/IGARSS.2018.8518512)
672

673 Nassar, R., Hill, T.G., McLinden, C.A., Wunch, D., Jones, D.B. and Crisp, D., 2017. Quantifying
674 CO2 emissions from individual power plants from space. *Geophysical Research Letters*, 44(19),
675 pp.10-045. DOI <https://doi.org/10.1002/2017GL074702>
676

677 Nassar, R., Mastrogiacomo, J.P., Bateman-Hemphill, W., McCracken, C., MacDonald, C.G., Hill,
678 T., O'Dell, C.W., Kiel, M. and Crisp, D., 2021. Advances in quantifying power plant CO2
679 emissions with OCO-2. *Remote Sensing of Environment*, 264, p.112579. DOI
680 <https://doi.org/10.1016/j.rse.2021.112579>
681

682 Nassar, R., Moeini, O., Mastrogiacomo, J.P., O'Dell, C.W., Nelson, R.R., Kiel, M., Chatterjee, A.,
683 Eldering, A. and Crisp, D., 2022. Tracking CO2 emission reductions from space: A case study at
684 Europe's largest fossil fuel power plant. *Frontiers in Remote Sensing*, 3, p.98. DOI
685 <https://doi.org/10.3389/frsen.2022.1028240>
686

687 O'Dell, C.W., Connor, B., Bösch, H., O'Brien, D., Frankenberg, C., Castano, R., Christi, M.,
688 Eldering, D., Fisher, B., Gunson, M. and McDuffie, J., 2012. The ACOS CO 2 retrieval algorithm–
689 Part 1: Description and validation against synthetic observations. *Atmospheric Measurement*
690 *Techniques*, 5(1), pp.99-121. DOI <https://doi.org/10.5194/amt-5-99-2012>

691

692 O'Dell, C.W., Eldering, A., Wennberg, P.O., Crisp, D., Gunson, M.R., Fisher, B., Frankenberg, C.,
693 Kiel, M., Lindqvist, H., Mandrake, L. and Merrelli, A., 2018. Improved retrievals of carbon dioxide
694 from Orbiting Carbon Observatory-2 with the version 8 ACOS algorithm. *Atmospheric*
695 *Measurement Techniques*, 11(12), pp.6539-6576. [DOI https://doi.org/10.5194/amt-11-6539-2018](https://doi.org/10.5194/amt-11-6539-2018)
696

697 Rodgers, C.D., 2000. *Inverse methods for atmospheric sounding: theory and practice* (Vol. 2).
698 World scientific.

699

700 Reuter, M., Buchwitz, M., Schneising, O., Krautwurst, S., O'Dell, C.W., Richter, A., Bovensmann,
701 H. and Burrows, J.P., 2019. Towards monitoring localized CO₂ emissions from space: co-located
702 regional CO₂ and NO₂ enhancements observed by the OCO-2 and S5P satellites. *Atmospheric*
703 *Chemistry and Physics*, 19(14), pp.9371-9383. [DOI https://doi.org/10.5194/acp-19-9371-2019](https://doi.org/10.5194/acp-19-9371-2019)
704

705 Sierk, B., Bézy, J.L., Löscher, A. and Meijer, Y., 2019, July. The European CO₂ Monitoring
706 Mission: observing anthropogenic greenhouse gas emissions from space. In *International*
707 *Conference on Space Optics—ICSO 2018* (Vol. 11180, pp. 237-250). SPIE. [DOI https://doi.org/](https://doi.org/10.1117/12.2535941)
708 [10.1117/12.2535941](https://doi.org/10.1117/12.2535941)
709

710 Taylor, T.E., O'Dell, C.W., Baker, D., Bruegge, C., Chang, A., Chapsky, L., Chatterjee, A., Cheng,
711 C., Chevallier, F., Crisp, D. and Dang, L., 2023. Evaluating the consistency between OCO-2 and
712 OCO-3 XCO₂ estimates derived from the NASA ACOS version 10 retrieval

713 algorithm. *Atmospheric Measurement Techniques Discussions*, 2023, pp.1-61. [DOI](#)

714 <https://doi.org/10.5194/amt-16-3173-2023>

715

716 Thorpe, A.K., Frankenberg, C., Thompson, D.R., Duren, R.M., Aubrey, A.D., Bue, B.D., Green,
717 R.O., Gerilowski, K., Krings, T., Borchardt, J. and Kort, E.A., 2017. Airborne DOAS retrievals of
718 methane, carbon dioxide, and water vapor concentrations at high spatial resolution: application to

719 AVIRIS-NG. *Atmospheric Measurement Techniques*, 10(10), pp.3833-3850. [DOI](#)

720 <https://doi.org/10.5194/amt-10-3833-2017>

721

722 Van Geffen, J., Boersma, K.F., Eskes, H., Sneep, M., Ter Linden, M., Zara, M. and Veeffkind, J.P.,
723 2020. S5P TROPOMI NO₂ slant column retrieval: Method, stability, uncertainties and comparisons

724 with OMI. *Atmospheric Measurement Techniques*, 13(3), pp.1315-1335. [DOI](#)

725 <https://doi.org/10.5194/amt-13-1315-2020>

726

727 Varon, D.J., Jacob, D.J., McKeever, J., Jervis, D., Durak, B.O., Xia, Y. and Huang, Y., 2018.

728 Quantifying methane point sources from fine-scale satellite observations of atmospheric methane
729 plumes. *Atmospheric Measurement Techniques*, 11(10), pp.5673-5686. [DOI](#)

730 <https://doi.org/10.5194/amt-11-5673-2018>